



## Article

# Theoretical Insights into the Hydrogen Evolution Reaction on the Ni<sub>3</sub>N Electrocatalyst

Russell W. Cross, Sachin R. Rondiya  and Nelson Y. Dzade \* 

School of Chemistry, Cardiff University, Main Building, Park Place, Cardiff CF10 3AT, UK; crossrw@cardiff.ac.uk (R.W.C.); RondiyaS@cardiff.ac.uk (S.R.R.)

\* Correspondence: DzadeNY@cardiff.ac.uk

**Abstract:** Ni-based catalysts are attractive alternatives to noble metal electrocatalysts for the hydrogen evolution reaction (HER). Herein, we present a dispersion-corrected density functional theory (DFT-D3) insight into HER activity on the (111), (110), (001), and (100) surfaces of metallic nickel nitride (Ni<sub>3</sub>N). A combination of water and hydrogen adsorption was used to model the electrode interactions within the water splitting cell. Surface energies were used to characterise the stabilities of the Ni<sub>3</sub>N surfaces, along with adsorption energies to determine preferable sites for adsorbate interactions. The surface stability order was found to be (111) < (100) < (001) < (110), with calculated surface energies of 2.10, 2.27, 2.37, and 2.38 Jm<sup>−2</sup>, respectively. Water adsorption was found to be exothermic at all surfaces, and most favourable on the (111) surface, with E<sub>ads</sub> = −0.79 eV, followed closely by the (100), (110), and (001) surfaces at −0.66, −0.65, and −0.56 eV, respectively. The water splitting reaction was investigated at each surface to determine the rate determining Volmer step and the activation energies (E<sub>a</sub>) for alkaline HER, which has thus far not been studied in detail for Ni<sub>3</sub>N. The E<sub>a</sub> values for water splitting on the Ni<sub>3</sub>N surfaces were predicted in the order (001) < (111) < (110) < (100), which were 0.17, 0.73, 1.11, and 1.60 eV, respectively, overall showing the (001) surface to be most active for the Volmer step of water dissociation. Active hydrogen adsorption sites are also presented for acidic HER, evaluated through the ΔG<sub>H</sub> descriptor. The (110) surface was shown to have an extremely active Ni–N bridging site with ΔG<sub>H</sub> = −0.05 eV.

**Keywords:** hydrogen evolution reaction (HER); nickel nitride (Ni<sub>3</sub>N); water splitting; density functional theory (DFT)



**Citation:** Cross, R.W.; Rondiya, S.R.; Dzade, N.Y. Theoretical Insights into the Hydrogen Evolution Reaction on the Ni<sub>3</sub>N Electrocatalyst. *Catalysts* **2021**, *11*, 716. <https://doi.org/10.3390/catal11060716>

Academic Editor: Oleg Vladislavovich Levin

Received: 14 May 2021

Accepted: 5 June 2021

Published: 8 June 2021

**Publisher's Note:** MDPI stays neutral with regard to jurisdictional claims in published maps and institutional affiliations.



**Copyright:** © 2021 by the authors. Licensee MDPI, Basel, Switzerland. This article is an open access article distributed under the terms and conditions of the Creative Commons Attribution (CC BY) license (<https://creativecommons.org/licenses/by/4.0/>).

## 1. Introduction

Hydrogen is fast becoming the best conceivable fuel to replace our damaging fossil fuel technologies. The transition to a hydrogen economy, however, requires efficient and economical ways of large-scale production of hydrogen to provide resources to all. Currently, steam reforming leads the way for industry; however, this is not a carbon-free process and results in the production of CO and CO<sub>2</sub> [1]. One promising method of obtaining hydrogen is through electrochemical water splitting [2,3]. This redox reaction breaks down to two half equations: the hydrogen evolution reaction (HER) and oxygen evolution reaction (OER). Pt electrodes are, at present, the best performing for HER; however, this expensive noble metal is not abundant enough to provide water splitting cells on a worldwide scale [4,5]. This introduces the urgent need for cheaper and more abundant alternatives. Much research has gone into using earth abundant transition metals to significantly reduce the cost of water splitting cells. Some promising materials have surfaced which have come close to the performance of Pt metals, such as transition metal sulphides (MoS<sub>2</sub> [6,7], WS<sub>2</sub> [8,9]), phosphides (FeP [10], CoP [11], Ni<sub>2</sub>P [12]), (oxy)hydroxides (Ni(OH)<sub>2</sub> [13,14], CoO(OH)<sub>2</sub> [15]), and transition metal carbides (Mo<sub>2</sub>C [16]). Transition metal nitrides (Mo<sub>2</sub>N [17], TiN [18], Ni<sub>3</sub>N [19]) have also been suggested recently, and much traction has grown with research of these materials.

Pure nickel catalysts such as Ni(111) have been shown to be active, although they do not present activities close to the benchmark Pt/C catalyst, but have prompted research into Ni-based subsidiaries [12]. Ni-based materials are strong candidates to replace expensive Pt for the hydrogen evolution reaction (HER) due to their low cost and strong corrosion resistance in alkaline media [20–24]. For instance, Strasser's group recently derived dealloyed metal–oxide hybrid IrNi@IrO<sub>x</sub> core–shell NPs, which provide substantial advances towards more efficient and less expensive electrocatalytic water splitting [25]. Dai et al. also synthesized a NiO/Ni-CNT heterostructured catalyst, which showed good resistance to alkaline media, performing consistently for over 24 h [26]. Several Ni-hydroxides [27], oxides [28], phosphides [29], nitrides [30], sulphides [31,32], and selenides [33] have shown the capability of providing efficient output for full water splitting compared to the benchmark Pt- and IrO<sub>2</sub>-based electrocatalysts.

Nickel nitride (Ni<sub>3</sub>N) is one such example of a Ni-based material which has shown good HER characteristics, having consistent performance over 12 h of runtime and > 5000 cycles [34]. Although it has been shown to be promising in fields such as lithium-ion batteries [35,36], it was first tested for HER activity by Shalom et al., who found it exhibited an extremely low overpotential of 50 mV when supported on Ni foam [19]. It was suggested this activity could be due to a presence of Ni(OH)<sub>2</sub> upon the surface. Ni<sub>3</sub>N has since been investigated in acidic media, with an H<sub>2</sub>SO<sub>4</sub> electrolyte by Ding et al. [34] who used XPS to show satellite Ni–O bonds present on the catalyst surface. However, this was removed after etching of the surface, and XRD confirmed Ni<sub>3</sub>N was the major product phase. Ding et al. also studied Ni<sub>3</sub>N with DFT calculations and ascribed the inherent activity to the Gibbs free energy of hydrogen adsorption ( $\Delta G_H^*$ ) values for hydrogen adsorption, whereby a value closer to zero is correlated to a higher activity catalyst. When a nanosheet with exposed (001) facets was tested, an optimal value of 0.065 eV was found for  $\Delta G_H^*$ .

Whilst  $\Delta G_H^*$  is a good descriptor for acidic environments, the initial Volmer step of adsorption is different when comparing with alkaline environments—it is instead water, which is dissociatively adsorbed onto the surface as OH\* and H\*, as opposed to a simple H adsorption [37,38]. Thus far, no studies have been dedicated to unravelling the mechanism of water adsorption and dissociation kinetics (the Volmer step) of HER on Ni<sub>3</sub>N surfaces. These insights are, however, essential to understand the HER activity of Ni<sub>3</sub>N and rationally engineer it to achieve improved HER performance. The present study aims to fill these gaps by investigating both molecular and dissociative water adsorption to the commonly observed low-index (111), (110), (001), and (100) surfaces of Ni<sub>3</sub>N [39,40]. Water adsorption is found to be exothermic atop all surfaces, binding via O–Ni interactions at all surfaces. From the water dissociation of the Volmer step, activation energies have been predicted, finding the (001) surface to be most active, whilst the (100) is the least. Hydrogen adsorption has also been investigated at all surfaces, with the most active sites for the Heyrovsky and Tafel steps presented.

## 2. Results and Discussion

### 2.1. Bulk and Surface Characterisation of Ni<sub>3</sub>N

Ni<sub>3</sub>N crystallised in the hexagonal Fe<sub>3</sub>N-type structure (Figure 1a) of the space group P6<sub>3</sub>22. From full geometry optimisation, the unit cell parameters were predicted to be  $a = b = 4.571$  Å and  $c = 4.262$  Å, which were in good agreement with previous experimental and DFT studies [34,41]. The material contained Ni–N bonds of length 1.87 Å, which also corresponded well to experimental values of 1.89 Å [41]. From the partial density of states (PDOS) diagram (Figure 1b), it can be seen that Ni<sub>3</sub>N is a metallic conductor, with Ni-*d* orbitals dominating states at the Fermi level [34].

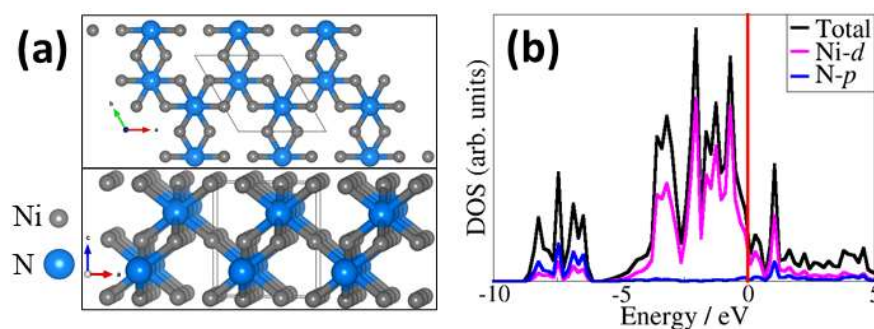


**Figure 1.** (a) Top and side views of the bulk  $\text{Ni}_3\text{N}$  crystal structure. (b) PDOS of bulk  $\text{Ni}_3\text{N}$ , showing metallic character through fermi level occupation at 0 eV.

The low-index (111), (110), (001), and (100)  $\text{Ni}_3\text{N}$  surfaces (Figure 2) created from the fully relaxed bulk structure were optimised to ascertain their relative stabilities. The  $\text{Ni}_3\text{N}$  (111) and (110) are commonly observed through experimental syntheses and are therefore shown to be active for the hydrogen evolution reaction alongside the (001) surface [39,40,42]. The  $\text{Ni}_3\text{N}$ (100) surface is also presented, as its surface energy ( $\gamma$ ) was calculated to be competitive with that of the (111) and (110) surfaces. The surface energies were found in the order of (111) < (100) < (001) < (110), with values of 2.10, 2.27, 2.37, and 2.38  $\text{J m}^{-2}$ , respectively.

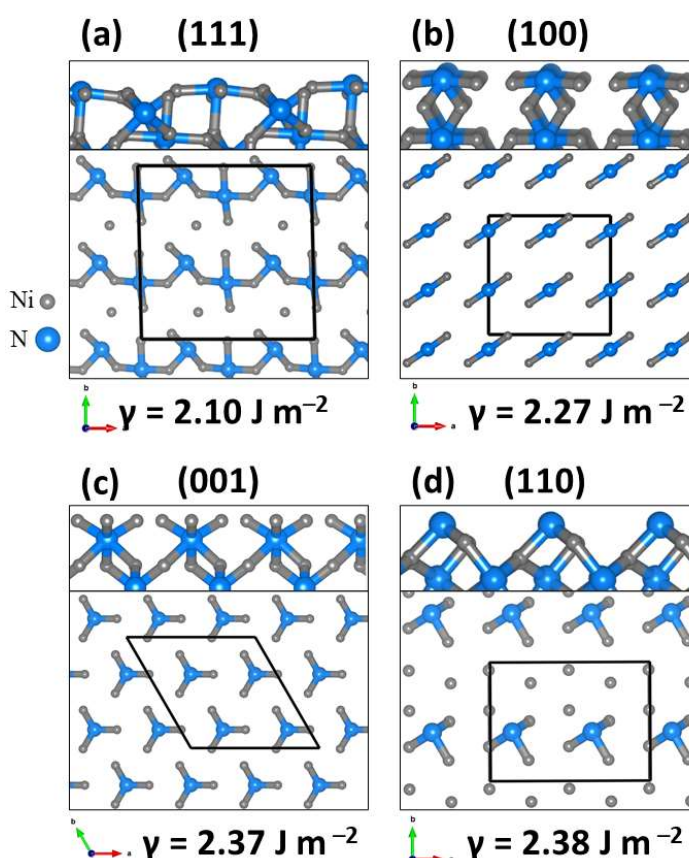


**Figure 2.** Side and top views of (a)  $\text{Ni}_3\text{N}$ (111), (b) (100), (c) (001), and (d) (110) surface terminations. Listed below each are the respective surface energies ( $\gamma$ ).

The Ni/N surface ratio of the (111) surface was 5:1, leading to an electron-deficient surface. The (110) surface, although Ni-rich, contained low-coordination, adatom-like nitrogen sites. This site was, therefore, predicted to be heavily preferable for adsorption

of water and hydrogen. Two terminations existed for the (001) surface, whereby the Ni-rich termination was chosen over the N-terminated, as previous studies have shown its increased activity in acidic conditions [34]. As such, only Ni sites were accessible across the slab. The  $\text{Ni}_3\text{N}(100)$  surface had a flat structure, and contained a higher concentration of N-sites than the (111), (110), and (001) surfaces, with a surface Ni/N atomic ratio of 2:1. Each Ni was in an equivalent position and bound to a single surface N.

## 2.2. Molecular Water Adsorption to $\text{Ni}_3\text{N}(111)$ , (110), (001), and (100) Surfaces

The most stable  $\text{H}_2\text{O}$  adsorption configuration for each surface is shown in Figure 3a–d. Water was found to preferentially adsorb to the Ni top site at all surfaces via the O atom. The ZPE-corrected adsorption energies, structural parameters including bond distances, bond angles, and O–H stretching vibrational modes for molecular water adsorption, are listed in Table 1. Water adsorption at the  $\text{Ni}_3\text{N}(111)$  surface was calculated to be exothermic, releasing  $E_{\text{ads}}^0 = -0.77$  eV, and contained a Ni–O bond length of 2.145 Å between adsorbed water and the surface site. Both O–H bonds remained close to values of molecular water at 0.983 and 0.973 Å. One O–H was translated towards a surface Ni to form a weak interaction, hence stabilising the system. This also caused a slight increase in the H–O–H angle from 104.5° to 105.6°. The stretching O–H modes of adsorbed water were also calculated to be 3818 and 3687  $\text{cm}^{-1}$ , corresponding to the symmetric and asymmetric modes, respectively. A decrease in the O–H stretching modes compared to the gas phase  $\text{H}_2\text{O}$  molecule (3987 and 3865  $\text{cm}^{-1}$ ) also indicated that O–H bonds were somewhat activated. Bader charge analyses of the interacting surface site ( $q(\text{Ni})$ ) and of the adsorbed water ( $q(\text{H}_2\text{O})$ , Table 1) showed that the  $\text{H}_2\text{O}$  molecule transferred a charge of 0.031  $e^-$  to the surface upon adsorption. Consistent with the small charge transfers, our differential charge density isosurface analysis (Figure 3e–h) revealed only small changes in the surface electron density, with a small accumulation at one hydrogen. This is suggestive of weak hydrogen bonding interactions with the surface. Since the first and rate-determining step of HER is the removal of hydrogen from water (Volmer step), a strong interaction between hydrogen and the surface, and slight activation of water, may prove to increase activity.

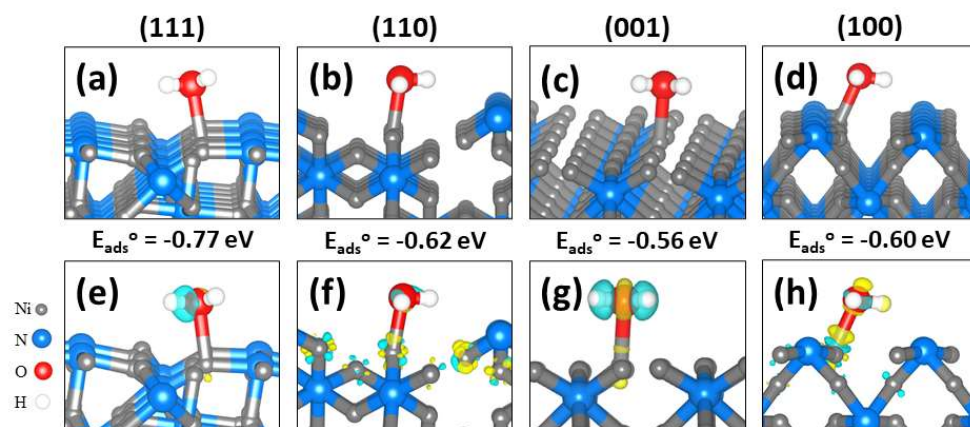


**Figure 3.** Lowest energy molecular water adsorption geometry on  $\text{Ni}_3\text{N}$  (111), (110), (001), and (100) surfaces (a–d), with corresponding ZPE-corrected adsorption energies ( $E_{\text{ads}}^0$ ). Each image is displayed with isosurface below (e–h), where accumulation is in cyan, and depletion in yellow. The depletion/accumulation levels were  $\pm 0.0224$  eV/Å<sup>3</sup>, as implemented in VESTA.



**Table 1.** ZPE-corrected adsorption energies ( $E_{ads}^o$ ), distance between water and surface Ni (Ni–O), O–H bond length in water, bond angles of water ( $\phi$ ), and vibrational frequency of the symmetric and asymmetric stretch O–H stretches of water (where the molecular values were 3988 and 3866  $\text{cm}^{-1}$ ). Bader charges of the Ni active site before (clean) and after ( $\text{H}_2\text{O}_{ads}$ ) adsorption are included, as well as the Bader charge of adsorbed water ( $q(\text{H}_2\text{O})$ ), where  $q(\text{H}_2\text{O})$  of molecular water was 0.

Surface	$E_{ads}^o$ (eV)	$d(\text{Ni–O})$ (Å)	$d(\text{O–H})$ (Å)	$\phi(\text{H–O–H})$ (°)	$\nu$ ( $\text{cm}^{-1}$ )	$q(\text{Ni})$ ( $e^-$ )		$q(\text{H}_2\text{O})$ ( $e^-$ )
						Clean	$\text{H}_2\text{O}_{ads}$	
(111)	−0.77	2.145	0.973, 0.983	105.6	3818, 3687	0.450	0.548	0.031
(110)	−0.62	2.047	0.981, 0.987	103.8	3744, 3640	0.214	0.354	0.042
(100)	−0.60	2.122	0.980, 0.982	104.1	3811, 3699	0.241	0.396	0.045
(001)	−0.56	2.085	0.983, 0.986	104.5	3660, 3532	0.184	0.340	0.027

Molecular adsorption of water on the  $\text{Ni}_3\text{N}(110)$  surface at the Ni site released an adsorption energy of −0.62 eV. The interacting Ni–O distance was calculated at 2.047 Å, along with the O–H distances at 0.987 and 0.981 Å and  $\phi(\text{H–O–H})$  angle of 103.8°. The O–H stretching vibrational frequencies decreased to 3744 and 3640  $\text{cm}^{-1}$ , indicating a weakening of O–H bonds. Water adsorbed to an N top site on the  $\text{Ni}_3\text{N}(001)$  Ni terminated surface, with an exothermic adsorption energy of  $E_{ads}^o = -0.56$  eV. The Ni–O bond distance was 2.085 Å, similar to geometries at the previously simulated surfaces. There was also minimal change at the O–H distances, which were predicted to be 0.983 and 0.986 Å, which was the same case for the H–O–H angle at 104.5°. It is worth noting that focus was on the Ni terminated surface due to the inability of the N terminated surface to adsorb water. A physisorbed state is preferred, yielding exothermic adsorption energies in the range 0.09–0.29 eV.

The adsorption of water to the  $\text{Ni}_3\text{N}(100)$  surface released an adsorption energy of  $E_{ads}^o = -0.60$  eV, with the interacting Ni–O distance predicted at 2.122 Å. The O–H bond lengths were not disturbed or changed from molecular water, remaining at 0.980 and 0.982 Å, and the  $\phi(\text{H–O–H})$  angle remained similar (104.1°) to that of the gas phase. The symmetric and asymmetric O–H stretching modes, however, were slightly reduced to 3811 and 3699  $\text{cm}^{-1}$ , respectively. The lesser extent of activation of the O–H bond at the (100) surface was likely to affect its water splitting ability.

### 2.3. Dissociated Water Adsorption on $\text{Ni}_3\text{N}$

From each molecular water adsorption system, we identified the preferred dissociative adsorption geometries ( $\text{OH}_{ads} + \text{H}_{ads}$ ) of water by moving one of the hydrogen atoms to an adjacent site. The most stable dissociative water adsorption geometries are shown in Figure 4 (FS, Figure 4i–l). At the  $\text{Ni}_3\text{N}(111)$  surface, the OH species remained adsorbed at the top Ni site, whereas the dissociated H atom preferentially bound to an  $\text{Ni}_3$  site, releasing an adsorption of −0.65 eV (Figure 4a,e,i). The interacting Ni–O distance of the adsorbed OH species was reduced significantly from the molecularly adsorbed water (2.145 Å) to 1.839 Å, with the O–H distance calculated at 0.974 Å. The average Ni–H bond amongst the  $\text{Ni}_3$  site was 1.700 Å. Overall, the dissociation process was slightly endothermic, with a reaction energy ( $E_{rxn}$ ) of 0.14 eV. NEB calculations were performed to ascertain the transition state (Figure 4e–h, TS) along the minimum energy pathway to the dissociated state. Activation energy ( $E_a$ ) barriers for the dissociative step were also found (Figure 5) and were adjusted by the ZPE as with the molecular water systems. The TS in each case was confirmed to have a single imaginary frequency.

$E_a$  for water splitting was found to be 0.73 eV at the (111) surface. Hydrogen diffused away from water, whereby the transition state (TS) had hydrogen midway between O and Ni, before reaching the  $\text{Ni}_3$  hollow site (Figure 4e). Hydrogen was found to split to an adjacent N top site at the (110) surface (Figure 4i) and was likely favoured due to the low coordination of surface-N. O–H remained adsorbed at the top Ni site (Ni–O = 1.805 Å and O–H = 0.981 Å). The dissociated proton diffused to a N top site with a converged N–H bond distance of 1.024 Å.  $E_{rxn}$  was calculated to be 0.07 eV, thereby showing molecular

adsorption to be slightly favoured and an endothermic path overall for the Volmer step. A higher activation barrier of 1.11 eV had to be overcome for this reaction to occur. The TS structure had hydrogen midway between oxygen and nitrogen, partially stabilised by an adjacent surface Ni atom.

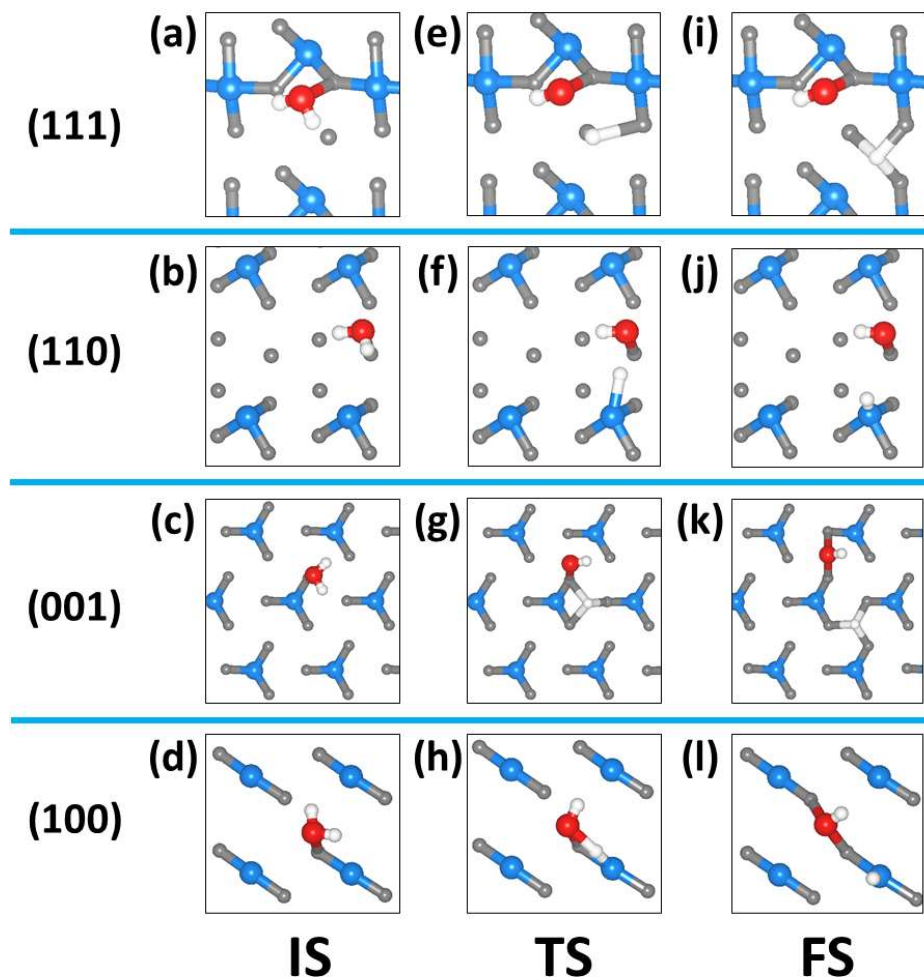


**Figure 4.** Overall water splitting pathways: from (a–d) the initial molecular water adsorption to (e–h) the corresponding transition state, and (i–l), the final H + OH co-adsorption on each of the Ni<sub>3</sub>N(111), (110), (001), and (100) surfaces.

Water dissociation on the (001) surface also led to an Ni<sub>3</sub> site for hydrogen diffusion, as with the (111) surface mechanism. This was due to the Ni-rich nature of the surface. An extremely stable binding site was found, with  $E_{\text{rxn}}$  found to be highly exothermic in nature at  $-0.64$  eV.  $E_{\text{rxn}}$  was further reduced not just by the stability of the H site, but OH also moved to form a bridging site, hence becoming more stable compared to the final (111) and (110) structures. The activation barrier was also extremely small, with  $E_a = 0.17$  eV. The low activation energy can be attributed to the inherent stabilization that occurred as hydrogen diffused to the binding site, with surface Ni acting to lower the energy of the transition state by interacting during diffusion. The Volmer step atop the Ni<sub>3</sub>N(100) surface had the hydrogen atom adsorbed at an N top site, with an N–H bond length of  $1.028$  Å. The OH species adsorbed at a bridge Ni site as with the (001) mechanism (N–O bonds were  $1.917$  and  $1.922$  Å). Compared to the (111) and (110) surface, water dissociation on the (100) surface was also found to be exothermic ( $E_{\text{rxn}} = -0.47$  eV) due to the strong interaction of OH at the bridge Ni site. Although the reaction was exothermic and thermodynamically favourable, it was kinetically limited due to the high activation barrier of  $1.60$  eV that had to be overcome. This suggests an extremely sluggish Volmer step ( $\text{H}_2\text{O} + \text{e}^- \rightarrow \text{OH}^- +$

$H_{ads}$ ) on the (100) surface, and thus poor HER activity, having the highest activation energy of the four surfaces.

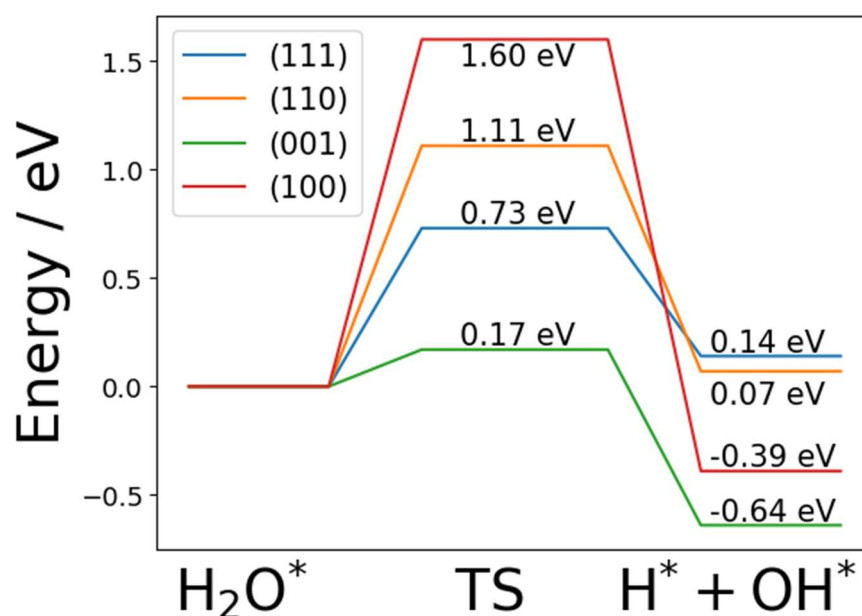


**Figure 5.** Reaction profile of the Volmer step (water dissociation) on  $Ni_3N$  (111), (110), and (100) surfaces, showing the ZPE-corrected activation energies.

#### 2.4. Hydrogen Adsorption to $Ni_3N$ Surfaces

Although the Volmer step is the first for HER in alkaline conditions, study of the consequential Tafel and Heyrovsky steps (combination of  $H^*$  to evolve  $H_2$ ) are, however, important to gain insights into the overall HER activity. The Gibbs free energy of hydrogen adsorption ( $\Delta G_H^*$ ) serves as a good descriptor for the HER activity, especially in acidic conditions [4]. Thermoneutral  $\Delta G_H^*$  values close to 0 eV indicate that hydrogen will stick neither too strongly nor weakly, hence allowing for recombination to  $H_2$  via the Tafel or Heyrovsky steps to be facile. The  $\Delta G_H^*$  values at the (111), (110), (100), and (001) surfaces were obtained via the following equation:  $\Delta G_H^* = \Delta E_H^* + \Delta ZPE - T\Delta S$ , where  $\Delta E_H^*$  is the 0 K, DFT calculated hydrogen adsorption energy, and  $\Delta ZPE$  and  $\Delta S$  are the zero-point energy and entropic corrections, respectively. Here,  $\Delta ZPE - T\Delta S$  was estimated to be 0.24 eV, on the basis of previous studies, with  $T = 300$  K [43].

The two most favourable structures for hydrogen adsorption at each surface were found and are shown in Figure 6. The only stable site found for the (001) surface was the  $Ni_3$  site, due to the lack of available N atoms at the termination. Hydrogen adsorption at the  $Ni_3N(111)$  surface showed strong exothermic, with  $\Delta G_H^* = -0.60$  eV at a top N site (Figure 6a) and  $-0.83$  eV at the  $Ni_3$  bridging site (Figure 6b). These two sites were highly unfavourable for HER as they may lead to a poisoning of the active sites when strongly adsorbed. The  $Ni_3$  site is a poisoning site for HER in various transition metal-based materials, such as  $Ni_2P$  [12,43–46]. These values indicate poor activity for the Tafel step of HER due to the strong adsorption to the catalyst surface.

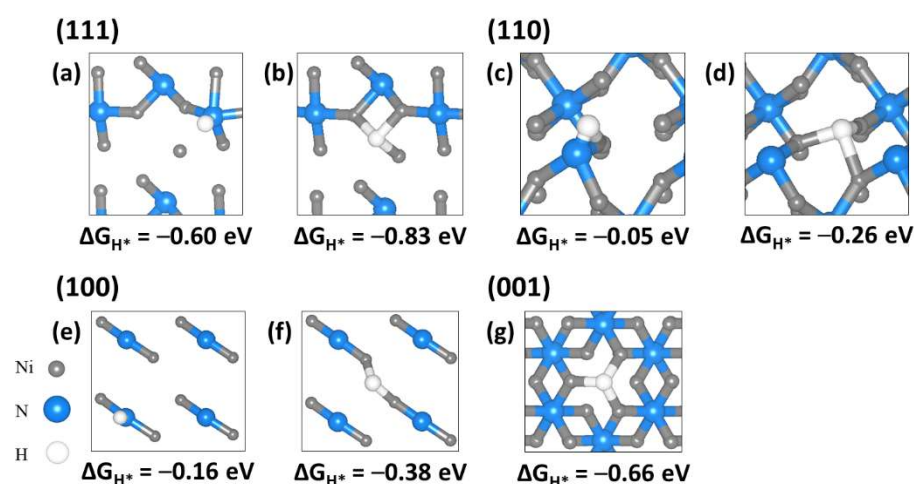


**Figure 6.** Two most optimal free energy of hydrogen adsorption ( $\Delta G_{H^*}$ ) structures on each of the  $Ni_3N$  surfaces. Where (a,b) are for the (111) surface, (c,d) for the (110), (e,f) for the (100), and (g) for the (001) surface.

At the  $Ni_3N(110)$  surface, a low  $\Delta G_{H^*}$  value was calculated at an Ni bridge site ( $-0.26$  eV). This was vastly better than for the similar state at the  $Ni_3N(111)$  surface. This was due to the reduced coordination number of the Ni site seen on the (111) surface leading to a stronger adsorption. An N top site was also tested; however, it converged to an N–Ni bridge site, with a highly optimal  $\Delta G_{H^*}$  value of  $-0.05$  eV. This was the most active site for acidic HER found across the four surfaces tested in this study. Due to the pure Ni nature of the Ni terminated (001) surface, hydrogen adsorption was limited to the favoured  $Ni_3$  site. This produced a strong binding site and low activity  $\Delta G_{H^*}$  predictor of  $-0.66$  eV, showing that although the Volmer step for the (001) surface was low, the activity was limited due to a possible poisoning of the site. Adsorption was also tested at the N terminated (001) surface, finding the extremely optimal Ni bridging site with  $\Delta G_{H^*} = -0.09$  eV, as observed previously [34].

The  $Ni_3N(100)$  surface also yielded competitive  $\Delta G_{H^*}$  values, calculated at  $-0.16$  and  $-0.38$  eV for the N top and Ni bridge sites, respectively. However, they did not compete with the  $\pm 0.10$  eV value of platinum [47]. It is noteworthy that our studies here also accounted for the London dispersion forces, which have been neglected in previous studies, leading to a more accurate picture of the binding interaction between the surface and hydrogen [34,48].

From the calculation of the most favourable HER routes for alkaline HER, the final hydrogen positions for the Volmer step at the (111), (110), (001), and (100) surfaces were the Ni bridge (Figure 4i), N topsite (Figure 4j), Ni bridge (Figure 4k), and N topsite (Figure 4l), respectively. The hydrogen adsorption was found to be a severe limitation towards high HER activity on the (111), (110), and (001) surfaces due to the highly negative  $\Delta G_{H^*}$  values of  $-0.83$ ,  $-0.62$ , and  $-0.66$  eV at the hydrogen resting spots. The lowest  $E_a$  in this study was found to be the (001) surface; however, it was not suggested as a highly active anode in the water splitting cell due to the sub-optimal  $\Delta G_{H^*}$  value, resulting in hydrogen sticking and poisoning the catalyst surface, hence reducing the rate at which the Tafel or Heyrovsky steps can occur.

These results suggest that efforts need to be made to engineer the surface properties of the  $Ni_3N$  electrocatalyst in order to achieve improved HER activity. Recent experimental efforts have shown that substitutional doping of Ni with other transition metals could vastly improve HER activity by providing alternative hydrogen adsorption sites to the (001) surface [49–51]. The formation of heterostructures by coupling  $Ni_3N$  with other materials, such as transition metal oxides [52,53] or nitrides [54,55], have also shown great promise. A  $NiMoN/Ni_3N$  heterostructure synthesized by Wang et al. [55] was demonstrated to exhibit



an extremely low overpotential of 28 mV at 10 mA cm<sup>−2</sup>, owing to the synergistic effect between the two materials that favoured charge transfer processes for water dissociation.

### 3. Conclusions

In conclusion, we provide a comprehensive DFT mechanistic insight into the Volmer step of HER on the Ni<sub>3</sub>N electrocatalyst through investigation of molecular and dissociative water adsorption on the (111), (110), (100), and (001) surfaces. Water was found to bind via the O atom to surface Ni sites in all cases. Adsorption was found to be exothermic for all surfaces; however, it was characterised by minimal interaction between the two, shown by our charge differential plots and small Bader charge values for H<sub>2</sub>O: 0.031, 0.042, 0.045, and 0.027 e<sup>−</sup> for the (111), (110), (100), and (001) surfaces, respectively. Activation energies for the rate-limiting Volmer step were found, and the Ni terminated (001) surface was shown to be the lowest at 0.17 eV, whilst it was found to be largest on the (100) surface, at E<sub>a</sub> = 1.60 eV. Hydrogen was found to split to a threefold Ni hollow site at the (001) site, whilst an adjacent N site for (100) was found. Furthermore, hydrogen adsorption was modelled at various Ni and N sites to yield valuable insight to the Tafel and Heyrovsky steps of the hydrogen evolution reaction. The resulting systems showed thermoneutral ΔG<sub>H</sub><sup>+</sup> values which were optimal for given HER applications, such as at the Ni–N bridge site atop the (110) surface, with ΔG<sub>H</sub><sup>+</sup> = −0.05 eV. Large negative values, such as −0.83 and −0.66 eV for the Ni bridging sites atop the (111) and (001) surfaces, resulted in a sticking of hydrogen and poisoning of the catalyst. Hence, we found it to be a source of inactivity as hydrogen will proceed to stick at these sites. Heterostructure formation and transition metal doping have been shown to improve the HER activity of Ni<sub>3</sub>N, and an ongoing DFT work aims to provide further detailed insight to the reasons behind these trends, as well as suggesting new combinations for facile hydrogen production.

### 4. Computational Details

Plane-wave-based DFT calculations were initiated through the Vienna ab initio Simulation Package (VASP) [56], using the Perdew Burke Ernzerhof (PBE) exchange correlation functional correction. A high energy cut-off of 600 eV and 10<sup>−6</sup> eV difference between ionic steps of the self-consistency process was used to represent convergence. Grimme's DFT-D3 scheme [57] was used to account Van der Waal's dispersion forces across each system. When optimising bulk Ni<sub>3</sub>N, we used a 5 × 5 × 5 Monkhorst-Pack K-point mesh to sample the Brillouin zone. For geometry optimisation of the surface slabs and the adsorbate surface systems, we utilized a 5 × 5 × 1 grid [58].

The METADISE code [59] was employed to obtain low miller index surfaces (111), (110), and (100) from the relaxed bulk material. For the (111), (100), and (001) surfaces, a (2 × 2) slab was used to ensure no adjacent interactions between supercells in the x-y-plane, while a (2 × 1) supercell was used for the (110) surface. Each surface contains a 15 Å vacuum region to ensure no interaction with periodic images in the z-direction, as well as a thickness of 10 Å to accurately mimic the catalytic material. The (001) surface was obtained from the bulk structure directly by adding a vacuum gap. For each surface termination, we obtained the surface energy (γ), which indicated the most stable arrangement for each surface. The following equation was used to calculate γ:

$$\gamma = \frac{E_{\text{surface}} - nE_{\text{bulk}}}{2A} \quad (1)$$

where  $E_{\text{surface}}$  is the energy of the naked surface,  $n$  is the number of repeating unit cells in the z-direction,  $E_{\text{bulk}}$  is the energy of the bulk system, and  $A$  is the surface area of the relaxed system.  $\gamma$  (Jm<sup>−2</sup>) indicates the energy required to cleave an infinite crystal to expose the termination; hence, a lower γ-value leads to a more favourable termination. The

following equation was used to determine the adsorption energies to the Ni<sub>3</sub>N surfaces, whereby the ZPE was included:

$$E_{ads}^o = (E_{surface+adsorbate} + ZPE) - E_{surface} - (E_{adsorbate} + ZPE) \quad (2)$$

where  $E_{surface+adsorbate}$  is the energy of the adsorbed water or hydrogen to the Ni<sub>3</sub>N slab,  $E_{surface}$  is the energy of the naked surface, and  $E_{adsorbate}$  is the energy of the respective adsorbate in the gas phase. Therefore, a negative  $E_{ads}^o$  (eV) value represents an exothermic, favourable adsorption, and vice versa.

Nudged elastic band (NEB) calculations were used to find transition states between molecular and dissociated water upon Ni<sub>3</sub>N. For each of the (111), (110), (001), and (100) surfaces, the most favourable molecular and dissociated systems, indicated by the most exothermic respective  $E_{ads}^o$  values, were taken as the start and end point with five images in between. The RMM-DIIS algorithm was then utilised, with a spring constant of  $-5 \text{ eV}/\text{\AA}$  between each image to find the transition state. Each was confirmed with vibrational frequency calculations as having a single imaginary frequency.

**Author Contributions:** Data curation, R.W.C.; formal analysis, R.W.C., S.R.R. and N.Y.D.; investigation R.W.C. and N.Y.D.; writing—original draft preparation, R.W.C.; writing—review and editing, S.R.R. and N.Y.D.; supervision, N.Y.D.; project administration, N.Y.D.; funding acquisition, N.Y.D. All authors have read and agreed to the published version of the manuscript.

**Funding:** This research was funded by the UK's Engineering and Physical Sciences Research Council (EPSRC), grant number EP/S001395/1.

**Data Availability Statement:** Information on the data that underpins the results presented here, including how to access them, can be found in the Cardiff University data catalogue at <http://doi.org/10.17035/d.2021.0136161101>, accessed on 8 June 2021.

**Acknowledgments:** R.W.C. acknowledges the College of Physical Sciences and Engineering, Cardiff University, for studentship. We also acknowledge the use of computational facilities of the Advanced Research Computing at Cardiff (ARCCA) Division, Cardiff University, and HPC Wales.

**Conflicts of Interest:** The authors declare no conflict of interest.

## References

1. Angeli, S.D.; Monteleone, G.; Giaconia, A.; Lemonidou, A.A. State-of-the-art catalysts for CH<sub>4</sub> steam reforming at low temperature. *Int. J. Hydrogen Energy* **2014**, *39*, 1979–1997. [CrossRef]
2. Duan, H.; Li, D.; Tang, Y.; He, Y.; Ji, S.; Wang, R.; Lv, H.; Lopes, P.P.; Paulikas, A.P.; Li, H.; et al. High-Performance Rh<sub>2</sub>P Electrocatalyst for Efficient Water Splitting. *J. Am. Chem. Soc.* **2017**, *139*, 5494–5502. [CrossRef] [PubMed]
3. El-Deab, M.S.; Ohsaka, T. Manganese Oxide Nanoparticles Electrodeposited on Platinum Are Superior to Platinum for Oxygen Reduction. *Angew. Chem. Int. Ed.* **2006**, *45*, 5963–5966. [CrossRef] [PubMed]
4. Noerskov, J.K.; Bligaard, T.; Logadottir, A.; Kitchin, J.R.; Chen, J.G.; Pandelov, S.; Stimming, U.; Nørskov, J.K.; Bligaard, T.; Logadottir, A.; et al. Trends in the Exchange Current for Hydrogen Evolution. *J. Electrochem. Soc.* **2005**, *152*, J23–J26. [CrossRef]
5. McKone, J.R.; Marinescu, S.C.; Brunschwig, B.S.; Winkler, J.R.; Gray, H.B. Earth-abundant hydrogen evolution electrocatalysts. *Chem. Sci.* **2014**, *5*, 865–878. [CrossRef]
6. Li, Y.; Wang, H.; Xie, L.; Liang, Y.; Hong, G.; Dai, H. MoS<sub>2</sub> Nanoparticles Grown on Graphene: An Advanced Catalyst for the Hydrogen Evolution Reaction. *J. Am. Chem. Soc.* **2011**, *133*, 7296–7299. [CrossRef]
7. Voiry, D.; Salehi, M.; Silva, R.; Fujita, T.; Chen, M.; Asefa, T.; Shenoy, V.B.; Eda, G.; Chhowalla, M. Conducting MoS<sub>2</sub> Nanosheets as Catalysts for Hydrogen Evolution Reaction. *Nano Lett.* **2013**, *13*, 6222–6227. [CrossRef]
8. Chen, T.-Y.; Chang, Y.-H.; Hsu, C.-L.; Wei, K.-H.; Chiang, C.-Y.; Li, L.-J. Comparative study on MoS<sub>2</sub> and WS<sub>2</sub> for electrocatalytic water splitting. *Int. J. Hydrogen Energy* **2013**, *38*, 12302–12309. [CrossRef]
9. Wu, Z.; Fang, B.; Bonakdarpour, A.; Sun, A.; Wilkinson, D.P.; Wang, D. WS<sub>2</sub> nanosheets as a highly efficient electrocatalyst for hydrogen evolution reaction. *Appl. Catal. B Environ.* **2012**, *125*, 59–66. [CrossRef]
10. Schipper, D.E.; Zhao, Z.; Thirumalai, H.; Leitner, A.P.; Donaldson, S.L.; Kumar, A.; Qin, F.; Wang, Z.; Grabow, L.C.; Bao, J.; et al. Effects of Catalyst Phase on the Hydrogen Evolution Reaction of Water Splitting: Preparation of Phase-Pure Films of FeP, Fe<sub>2</sub>P, and Fe<sub>3</sub>P and Their Relative Catalytic Activities. *Chem. Mater.* **2018**, *30*, 3588–3598. [CrossRef]
11. Jiao, L.; Zhou, Y.-X.; Jiang, H.-L. Metal–organic framework-based CoP/reduced graphene oxide: High-performance bifunctional electrocatalyst for overall water splitting. *Chem. Sci.* **2016**, *7*, 1690–1695. [CrossRef] [PubMed]

12. Liu, P.; Rodriguez, J.A. Catalysts for hydrogen evolution from the [NiFe] hydrogenase to the Ni<sub>2</sub>P(001) surface: The importance of ensemble effect. *J. Am. Chem. Soc.* **2005**, *127*, 14871–14878. [\[CrossRef\]](#) [\[PubMed\]](#)
13. Zhang, B.; Liu, J.; Wang, J.; Ruan, Y.; Ji, X.; Xu, K.; Chen, C.; Wan, H.; Miao, L.; Jiang, J. Interface engineering: The Ni(OH)<sub>2</sub>/MoS<sub>2</sub> heterostructure for highly efficient alkaline hydrogen evolution. *Nano Energy* **2017**, *37*, 74–80. [\[CrossRef\]](#)
14. Danilovic, N.; Subbaraman, R.; Strmcnik, D.; Chang, K.-C.; Paulikas, A.P.; Stamenkovic, V.R.; Markovic, N.M. Enhancing the Alkaline Hydrogen Evolution Reaction Activity through the Bifunctionality of Ni(OH)<sub>2</sub>/Metal Catalysts. *Angew. Chem. Int. Ed.* **2012**, *51*, 12495–12498. [\[CrossRef\]](#) [\[PubMed\]](#)
15. Subbaraman, R.; Tripkovic, D.; Chang, K.-C.; Strmcnik, D.; Paulikas, A.P.; Hirunsit, P.; Chan, M.; Greeley, J.; Stamenkovic, V.; Markovic, N.M. Trends in activity for the water electrolyser reactions on 3d M(Ni,Co,Fe,Mn) hydr(oxy)oxide catalysts. *Nat. Mater.* **2012**, *11*, 550. [\[CrossRef\]](#)
16. Chaitoglou, S.; Giannakopoulou, T.; Papanastasiou, G.; Tsoutsou, D.; Vavouliotis, A.; Trapalis, C.; Dimoulas, A. Cu vapor-assisted formation of nanostructured Mo<sub>2</sub>C electrocatalysts via direct chemical conversion of Mo surface for efficient hydrogen evolution reaction applications. *Appl. Surf. Sci.* **2020**, *510*, 145516. [\[CrossRef\]](#)
17. Ma, L.; Ting, L.R.L.; Molinari, V.; Giordano, C.; Yeo, B.S. Efficient hydrogen evolution reaction catalyzed by molybdenum carbide and molybdenum nitride nanocatalysts synthesized via the urea glass route. *J. Mater. Chem. A* **2015**, *3*, 8361–8368. [\[CrossRef\]](#)
18. Zhang, Q.; Wang, Y.; Wang, Y.; Al-Enizi, A.M.; Elzatahry, A.A.; Zheng, G. Myriophyllum-like hierarchical TiN@Ni<sub>3</sub>N nanowire arrays for bifunctional water splitting catalysts. *J. Mater. Chem. A* **2016**, *4*, 5713–5718. [\[CrossRef\]](#)
19. Shalom, M.; Ressnig, D.; Yang, X.; Clavel, G.; Feller, T.P.; Antonietti, M. Nickel nitride as an efficient electrocatalyst for water splitting. *J. Mater. Chem. A* **2015**, *3*, 8171–8177. [\[CrossRef\]](#)
20. Pu, Z.; Liu, Q.; Tang, C.; Asiri, A.M.; Sun, X. Ni<sub>2</sub>P nanoparticle films supported on a Ti plate as an efficient hydrogen evolution cathode. *Nanoscale* **2014**, *6*, 11031–11034. [\[CrossRef\]](#)
21. Tang, C.; Xie, L.; Sun, X.; Asiri, A.M.; He, Y. Highly efficient electrochemical hydrogen evolution based on nickel diselenide nanowall film. *Nanotechnology* **2016**, *27*, 20LT02. [\[CrossRef\]](#) [\[PubMed\]](#)
22. Zhu, Y.; Liu, T.; Li, L.; Song, S.; Ding, R. Nickel-based electrodes as catalysts for hydrogen evolution reaction in alkaline media. *Ionics* **2018**, *24*, 1121–1127. [\[CrossRef\]](#)
23. Zhang, J.; Wang, T.; Liu, P.; Liao, Z.; Liu, S.; Zhuang, X.; Chen, M.; Zschech, E.; Feng, X. Efficient hydrogen production on MoNi<sub>4</sub> electrocatalysts with fast water dissociation kinetics. *Nat. Commun.* **2017**, *8*, 15437. [\[CrossRef\]](#)
24. Song, F.; Li, W.; Han, G.; Sun, Y. Electropolymerization of Aniline on Nickel-Based Electrocatalysts Substantially Enhances Their Performance for Hydrogen Evolution. *ACS Appl. Energy Mater.* **2018**, *1*, 3–8. [\[CrossRef\]](#)
25. Nong, H.N.; Gan, L.; Willinger, E.; Teschner, D.; Strasser, P. IrOx core-shell nanocatalysts for cost- and energy-efficient electrochemical water splitting. *Chem. Sci.* **2014**, *5*, 2955–2963. [\[CrossRef\]](#)
26. Gong, M.; Zhou, W.; Tsai, M.-C.; Zhou, J.; Guan, M.; Lin, M.-C.; Zhang, B.; Hu, Y.; Wang, D.-Y.; Yang, J.; et al. Nanoscale nickel oxide/nickel heterostructures for active hydrogen evolution electrocatalysis. *Nat. Commun.* **2014**, *5*, 4695. [\[CrossRef\]](#)
27. Zhang, F.-S.; Wang, J.-W.; Luo, J.; Liu, R.-R.; Zhang, Z.-M.; He, C.-T.; Lu, T.-B. Extraction of nickel from NiFe-LDH into Ni<sub>2</sub>P@NiFe hydroxide as a bifunctional electrocatalyst for efficient overall water splitting. *Chem. Sci.* **2018**, *9*, 1375–1384. [\[CrossRef\]](#)
28. Yan, X.; Tian, L.; Chen, X. Crystalline/amorphous Ni/NiO core/shell nanosheets as highly active electrocatalysts for hydrogen evolution reaction. *J. Power Sources* **2015**, *300*, 336–343. [\[CrossRef\]](#)
29. Popczun, E.J.; McKone, J.R.; Read, C.G.; Biacchi, A.J.; Wiltrout, A.M.; Lewis, N.S.; Schaak, R.E. Nanostructured Nickel Phosphide as an Electrocatalyst for the Hydrogen Evolution Reaction. *J. Am. Chem. Soc.* **2013**, *135*, 9267–9270. [\[CrossRef\]](#)
30. Xing, Z.; Li, Q.; Wang, D.; Yang, X.; Sun, X. Self-supported nickel nitride as an efficient high-performance three-dimensional cathode for the alkaline hydrogen evolution reaction. *Electrochim. Acta* **2016**, *191*, 841–845. [\[CrossRef\]](#)
31. Jiang, N.; Tang, Q.; Sheng, M.; You, B.; Jiang, D.; Sun, Y. Nickel sulfides for electrocatalytic hydrogen evolution under alkaline conditions: A case study of crystalline NiS, NiS<sub>2</sub>, and Ni<sub>3</sub>S<sub>2</sub> nanoparticles. *Catal. Sci. Technol.* **2016**, *6*, 1077–1084. [\[CrossRef\]](#)
32. Chen, P.; Zhou, T.; Zhang, M.; Tong, Y.; Zhong, C.; Zhang, N.; Zhang, L.; Wu, C.; Xie, Y. 3D Nitrogen-Anion-Decorated Nickel Sulfides for Highly Efficient Overall Water Splitting. *Adv. Mater.* **2017**, *29*, 1701584. [\[CrossRef\]](#)
33. Wang, F.; Li, Y.; Shifa, T.A.; Liu, K.; Wang, F.; Wang, Z.; Xu, P.; Wang, Q.; He, J. Selenium-Enriched Nickel Selenide Nanosheets as a Robust Electrocatalyst for Hydrogen Generation. *Angew. Chem. Int. Ed.* **2016**, *55*, 6919–6924. [\[CrossRef\]](#)
34. Gao, D.; Zhang, J.; Wang, T.; Xiao, W.; Tao, K.; Xue, D.; Ding, J. Metallic Ni<sub>3</sub>N nanosheets with exposed active surface sites for efficient hydrogen evolution. *J. Mater. Chem. A* **2016**, *4*, 17363–17369. [\[CrossRef\]](#)
35. Wang, Y.; Fu, Z.-W.; Yue, X.-L.; Qin, Q.-Z. Electrochemical Reactivity Mechanism of Ni<sub>3</sub>N with Lithium. *J. Electrochem. Soc.* **2004**, *151*, E162–E167. [\[CrossRef\]](#)
36. Gillot, F.; Oró-Solé, J.; Palacín, M.R. Nickel nitride as negative electrode material for lithium ion batteries. *J. Mater. Chem.* **2011**, *21*, 9997–10002. [\[CrossRef\]](#)
37. Tang, Q.; Jiang, D. Mechanism of Hydrogen Evolution Reaction on 1T-MoS<sub>2</sub> from First Principles. *ACS Catal.* **2016**, *6*, 4953–4961. [\[CrossRef\]](#)
38. Zhang, J.; Wang, T.; Liu, P.; Liu, S.; Dong, R.; Zhuang, X.; Chen, M.; Feng, X. Engineering water dissociation sites in MoS<sub>2</sub> nanosheets for accelerated electrocatalytic hydrogen production. *Energy Environ. Sci.* **2016**, *9*, 2789–2793. [\[CrossRef\]](#)
39. Gao, M.; Chen, L.; Zhang, Z.; Sun, X.; Zhang, S. Interface engineering of the Ni(OH)<sub>2</sub>-Ni<sub>3</sub>N nanoarray heterostructure for the alkaline hydrogen evolution reaction. *J. Mater. Chem. A* **2018**, *6*, 833–836. [\[CrossRef\]](#)

40. Liu, Q.; Xie, L.; Qu, F.; Liu, Z.; Du, G.; Asiri, A.M.; Sun, X. A porous Ni<sub>3</sub>N nanosheet array as a high-performance non-noble-metal catalyst for urea-assisted electrochemical hydrogen production. *Inorg. Chem. Front.* **2017**, *4*, 1120–1124. [\[CrossRef\]](#)
41. Leineweber, A.; Jacobs, H.; Hull, S. Ordering of Nitrogen in Nickel Nitride Ni<sub>3</sub>N Determined by Neutron Diffraction. *Inorg. Chem.* **2001**, *40*, 5818–5822. [\[CrossRef\]](#)
42. Liu, T.; Li, M.; Jiao, C.; Hassan, M.; Bo, X.; Zhou, M.; Wang, H.-L. Design and synthesis of integrally structured Ni<sub>3</sub>N nanosheets/carbon microfibers/Ni<sub>3</sub>N nanosheets for efficient full water splitting catalysis. *J. Mater. Chem. A* **2017**, *5*, 9377–9390. [\[CrossRef\]](#)
43. Cross, R.W.; Dzade, N.Y. First-Principles Mechanistic Insights into the Hydrogen Evolution Reaction on Ni<sub>2</sub>P Electrocatalyst in Alkaline Medium. *Catalysts* **2020**, *10*, 307. [\[CrossRef\]](#)
44. Bai, Y.; Kirvassilis, D.; Xu, L.; Mavrikakis, M. Atomic and molecular adsorption on Ni(111). *Surf. Sci.* **2019**, *679*, 240–253. [\[CrossRef\]](#)
45. Nojima, A.; Yamashita, K. A theoretical study of hydrogen adsorption and diffusion on a W(110) surface. *Surf. Sci.* **2007**, *601*, 3003–3011. [\[CrossRef\]](#)
46. Hansen, M.H.; Stern, L.-A.; Feng, L.; Rossmeisl, J.; Hu, X. Widely available active sites on Ni<sub>2</sub>P for electrochemical hydrogen evolution – insights from first principles calculations. *Phys. Chem. Chem. Phys.* **2015**, *17*, 10823–10829. [\[CrossRef\]](#) [\[PubMed\]](#)
47. Wu, H.; Zuo, X.; Wang, S.-P.; Yin, J.-W.; Zhang, Y.-N.; Chen, J. Theoretical and experimental design of Pt-Co(OH)<sub>2</sub> electrocatalyst for efficient HER performance in alkaline solution. *Prog. Nat. Sci. Mater. Int.* **2019**, *29*, 356–361. [\[CrossRef\]](#)
48. Zhang, B.; Wang, J.; Liu, J.; Zhang, L.; Wan, H.; Miao, L.; Jiang, J. Dual-Descriptor Tailoring: The Hydroxyl Adsorption Energy-Dependent Hydrogen Evolution Kinetics of High-Valence State Doped Ni<sub>3</sub>N in Alkaline Media. *ACS Catal.* **2019**, *9*, 9332–9338. [\[CrossRef\]](#)
49. Zhang, J.; Liu, Y.; Li, J.; Jin, X.; Li, Y.; Qian, Q.; Wang, Y.; El-Harairy, A.; Li, Z.; Zhu, Y.; et al. Vanadium Substitution Steering Reaction Kinetics Acceleration for Ni<sub>3</sub>N Nanosheets Endows Exceptionally Energy-Saving Hydrogen Evolution Coupled with Hydrazine Oxidation. *ACS Appl. Mater. Interfaces* **2021**, *13*, 3881–3890. [\[CrossRef\]](#)
50. Li, R.-Q.; Liu, Q.; Zhou, Y.; Lu, M.; Hou, J.; Qu, K.; Zhu, Y.; Fontaine, O. 3D self-supported porous vanadium-doped nickel nitride nanosheet arrays as efficient bifunctional electrocatalysts for urea electrolysis. *J. Mater. Chem. A* **2021**, *9*, 4159–4166. [\[CrossRef\]](#)
51. Wang, M.; Ma, W.; Lv, Z.; Liu, D.; Jian, K.; Dang, J. Co-Doped Ni<sub>3</sub>N Nanosheets with Electron Redistribution as Bifunctional Electrocatalysts for Efficient Water Splitting. *J. Phys. Chem. Lett.* **2021**, *12*, 1581–1587. [\[CrossRef\]](#)
52. Liu, X.; Guo, Y.; Wang, P.; Wu, Q.; Zhang, Q.; Rozhkova, E.A.; Wang, Z.; Liu, Y.; Zheng, Z.; Dai, Y.; et al. Synthesis of Synergistic Nitrogen-Doped NiMoO<sub>4</sub>/Ni<sub>3</sub>N Heterostructure for Implementation of an Efficient Alkaline Electrocatalytic Hydrogen Evolution Reaction. *ACS Appl. Energy Mater.* **2020**, *3*, 2440–2449. [\[CrossRef\]](#)
53. Niu, S.; Fang, Y.; Zhou, J.; Cai, J.; Zang, Y.; Wu, Y.; Ye, J.; Xie, Y.; Liu, Y.; Zheng, X.; et al. Manipulating the water dissociation kinetics of Ni<sub>3</sub>N nanosheets via in situ interfacial engineering. *J. Mater. Chem. A* **2019**, *7*, 10924–10929. [\[CrossRef\]](#)
54. Huang, H.; Yu, C.; Han, X.; Li, S.; Cui, S.; Zhao, C.; Huang, H.; Qiu, J. Interface Engineering of Ni<sub>3</sub>N@Fe<sub>3</sub>N Heterostructure Supported on Carbon Fiber for Enhanced Water Oxidation. *Ind. Eng. Chem. Res.* **2017**, *56*, 14245–14251. [\[CrossRef\]](#)
55. Hua, W.; Sun, H.; Liu, H.; Li, Y.; Wang, J.-G. Interface engineered NiMoN/Ni<sub>3</sub>N heterostructures for enhanced alkaline hydrogen evolution reaction. *Appl. Surf. Sci.* **2021**, *540*, 148407. [\[CrossRef\]](#)
56. Kresse, G.; Furthmüller, J. Efficient iterative schemes for ab initio total-energy calculations using a plane-wave basis set. *Phys. Rev. B* **1996**, *54*, 11169–11186. [\[CrossRef\]](#) [\[PubMed\]](#)
57. Perdew, J.P.; Burke, K.; Ernzerhof, M. Generalized Gradient Approximation Made Simple. *Phys. Rev. Lett.* **1996**, *77*, 3865–3868. [\[CrossRef\]](#)
58. Grimme, S.; Antony, J.; Ehrlich, S.; Krieg, H. A consistent and accurate ab initio parametrization of density functional dispersion correction (DFT-D) for the 94 elements H-Pu. *J. Chem. Phys.* **2010**, *132*, 154104. [\[CrossRef\]](#) [\[PubMed\]](#)
59. Watson, G.W.; Kelsey, E.T.; de Leeuw, N.H.; Harris, D.J.; Parker, S.C. Atomistic simulation of dislocations, surfaces and interfaces in MgO. *J. Chem. Soc. Faraday Trans.* **1996**, *92*, 433–438. [\[CrossRef\]](#)